

# Measuring the Effects of Artificial Viscosity in SPH Simulations of Rotating Fluid Flows

P. A. Taylor<sup>1,2,3\*</sup> and J. C. Miller<sup>1,4\*</sup>

<sup>1</sup>*Department of Physics (Astrophysics), University of Oxford, Keble Road, Oxford OX1 3RH, UK*

<sup>2</sup>*African Institute for Mathematical Sciences, 6-8 Melrose Road, Muizenberg 7945, South Africa*

<sup>3</sup>*Department of Radiology, UMDNJ-New Jersey Medical School, ADMC 5, Suite 575, 30 Bergen St., Newark, NJ 07103, USA*

<sup>4</sup>*SISSA, International School for Advanced Studies, & INFN, Via Bonomea 265, 34136 Trieste, Italy*

draft version

## ABSTRACT

A commonly cited drawback of SPH is the introduction of spurious shear viscosity by the artificial viscosity term in situations involving rotation. Existing approaches for quantifying its effect include approximate analytic formulae and disc-averaged behaviour in specific ring-spreading simulations, based on the kinematic effects produced by the artificial viscosity. These methods have disadvantages, in that they typically are applicable to a very small range of physical scenarios, have a large number of simplifying assumptions, and often are tied to specific SPH formulations which do not include corrective (e.g., Balsara) or time-dependent artificial viscosity terms. In this study we have developed a simple, generally applicable and practical technique for evaluating the local effect of artificial viscosity directly from the creation of specific entropy for each SPH particle. This local approach is simple and quick to implement, and it allows a detailed characterization of viscous effects as a function of position. Several advantages of this method are discussed, including its ease in evaluation, its greater accuracy and its broad applicability. In order to compare this new method with existing ones, simple disc flow examples are used. Even in these basic cases, the very roughly approximate nature of the previous methods is shown. Our local method provides a detailed description of the effects of the artificial viscosity throughout the disc, even for extended examples which implement Balsara corrections. As a further use of this approach, explicit dependencies of the effective viscosity in terms of SPH and flow parameters are estimated from the example cases. In an appendix, a method for the initial placement of SPH particles is discussed which is very effective in reducing numerical fluctuations.

**Key words:** Hydrodynamic models – Viscosity – Accretion and accretion discs

## 1 INTRODUCTION

Continued advances in computing power and availability have led to an increasingly important role for numerical simulations in understanding hydrodynamical phenomena, and astrophysics provides a particular range of interesting applications. High-resolution, multidimensional studies frequently include an ambitious amount of physics in order to reproduce the dynamics of a system with sufficient accuracy. However, numerical artefacts and limitations are necessarily present and must be understood as fully as possible to appreciate the actual physics in the systems being represented.

Non-physical features enter *ab initio* into all hydro-

dynamic simulations simply because of the discretisation of a ‘continuous’ fluid (which is itself discrete, of course, but on very small scales). The two types of method developed for this task have very different structures: Lagrangian methods follow moving fluid elements, while Eulerian methods compute flow properties on a grid of points; additionally, there are ‘hybrid’ approaches, the so-called ALE (arbitrary Lagrangian-Eulerian) schemes, e.g. the BETHEhydro code (Murphy & Burrows 2008). In this paper, we focus on the Lagrangian smoothed particle hydrodynamics (SPH) method, which has been widely used for modelling astrophysical phenomena (Gingold & Monaghan 1977; Lucy 1977). SPH has both advantages and disadvantages with respect to other numerical techniques. One main advantage is that it automatically adapts to following dynamic flows and arbitrary geometries, without the need for mesh refinement

\* E-mail: ptaylor@astro.ox.ac.uk (PT); jcm@astro.ox.ac.uk (JCM)

or other readjustment techniques required with Eulerian-based codes. Furthermore, the energy equation is solved in the local comoving frame of each fluid element, giving a direct implementation of the first law of thermodynamics.

In modelling fluids by means of SPH particles, most SPH codes have included an artificial viscosity term, both for making the ensemble of discrete particles behave more like a continuum (in continuous regions of the flow) and for handling shock discontinuities which may arise during the course of a simulation. Methods for shock-handling with Riemann solvers have also been implemented in SPH (Inutsuka 2002; Cha & Whitworth 2003); these approaches have both advantages and disadvantages. Here, we focus on the artificial viscosity methods as used in standard SPH formulations. As well as having beneficial effects, artificial viscosity can also introduce unwanted numerical artefacts, among which spurious shearing torques in rotating flows are particularly troublesome (see, for example, Flebbe et al. (1994)). Techniques such as the Balsara correction (described in the next section) have been developed for counteracting this. Typically, SPH prescriptions for artificial viscosity are a composite of both bulk and shear viscosity components, but act as a source of dissipation primarily related to shear when modelling rotating fluid flows. It is important to have some quantitative measure of how large the effects of this are, whether one is dealing with problems having no intrinsic shear viscosity or whether there is also a real, physical shear viscosity; in either case, any numerical viscosity should be suitably negligible (unless one is trying to use an artificial viscosity to actually model a physical viscosity, see e.g., Lodato & Price (2010)). We focus here on two standard artificial viscosity prescriptions, with and without the Balsara correction.

The main objective of this paper is to advocate monitoring local entropy generation as a means for quantifying the residual effects of artificial viscosity in regular flows not involving shocks. Our method is completely general, but we test it out by applying it to frequently-used idealized test problems involving isothermal discs and compare its performance on these with that of other alternative methods. Two main types of approach have been used previously, both of which measure the kinematic effect of the artificial viscosity and relate it to an effective viscosity coefficient,  $\nu$ . Firstly, there are the empirical ‘ring-spreading’ tests (Lüst 1952; Lynden-Bell & Pringle 1974; Flebbe et al. 1994; Murray 1996; Speith & Riffert 1999). These are based on the analytic relations for the kinematic contribution of the artificial viscosity to disc-averaged behaviour, with assumptions of an isothermal equation of state and a small viscosity (so as not to generate large radial flow) that is constant across the disc. In practice, these tests can only be performed in two dimensions, as the thermal pressure of the fluid is zeroed to isolate the viscosity term in the equations of motion. These methods also require post-simulation fitting of averaged results. Secondly, analytic approximations have been developed relating  $\nu$  to SPH and disc parameters (Murray 1996; Lodato & Price 2010). These relations are generally derived for specific formulations of SPH artificial viscosity with the quadratic term set to zero. Various additional assumptions include having constant smoothing lengths (in the continuum limit) and particular SPH particle kernel shapes, as well as considerations that the viscosity is active for both receding and approaching particles.

Both of these kinds of existing approach involve restrictive assumptions and neither may be applied to artificial viscosity prescriptions that include often-used ‘corrective’ terms, such as the Balsara method or time-dependent approaches (discussed below), which aim to reduce ‘excess’ shearing.

The technique presented here involves evaluating the effect of artificial viscosity in rotating flows directly from local entropy production (i.e. using the energy equation rather than the equation of motion). It does not assume any particular equation of state or rotation profile and also does not assume constancy of  $\nu$  or of smoothing lengths, or any particular artificial viscosity prescription. Moreover, it requires no special simulation setup and is directly calculable from standard SPH particle quantities. Impetus for this approach arises from the nature of the SPH method itself and its direct application of the first law of thermodynamics, noting that a clear understanding of entropy production is of great importance in numerical simulations. The technique is simple and quick to implement, and it allows a detailed characterization of the effects of the artificial viscosity as a function of position. Several advantages of this method over existing ones are discussed, including its ease in evaluation, its direct interpretation, its greater accuracy and its broad applicability, e.g., to arbitrary rotation profiles and equations of state.

For all of the simulations described here, we have utilised the public-release version of the Gadget-2 code (Springel 2005). While several artificial viscosity formulations of varying sophistication have been developed over the years, in this paper we focus mainly on the *method* of estimating the effects of this viscosity and therefore utilize only the relatively simple form that is standard in Gadget-2 (with and without the Balsara treatment, described below). However, the method itself is independent of viscosity prescription, and our aim is to apply it to a comparison of several other formulations in a forthcoming paper. Here, we begin by briefly reviewing in §2 the form of SPH equations used and considerations concerning the artificial viscosity; in §3, the ring-spreading test is described; in §4, both the motivation for and the general formulation of our local criterion for measuring the effective viscosity in rotating flows are described; in §5, example applications of our method in thin discs are given, and various simulations performed, for which the results of the local measures of viscosity are compared with those of the ring-spreading tests and existing analytic formulations; these results are then discussed in §6. Additionally, in Appendix A, we discuss the SPH particle setup used for our initial conditions, which is presented as a simple improvement to aid in reducing numerical effects and increasing the efficiency of convergence.

## 2 SPH, USING GADGET-2

In SPH a continuous fluid is sampled at a finite number of points, and discretised versions of the standard hydrodynamic equations of continuity, momentum (Euler) and the first law of thermodynamics (energy equation) are evolved, given respectively in their simplest form as:

$$0 = \frac{d}{dt}\rho + \rho\nabla\cdot\mathbf{v} \quad (1)$$

$$0 = \frac{d}{dt} \mathbf{v} + \frac{1}{\rho} \nabla P \quad (2)$$

$$0 = \frac{d}{dt} \epsilon - \frac{P}{\rho^2} \frac{d}{dt} \rho, \quad (3)$$

written with Lagrangian derivatives,  $d/dt = \partial/\partial t + \mathbf{v} \cdot \nabla$ , and with mass density,  $\rho$ ; velocity,  $\mathbf{v}$ ; thermal pressure,  $P$ ; and specific internal energy,  $\epsilon$ . The exact form of SPH implementations has continued to be refined over the decades; in this work, we have used the publicly-available SPH code, Gadget-2, the formulation of which is derived from a fluid Lagrangian and, importantly, directly conserves linear and angular momentum, entropy and energy (Springel & Hernquist 2002). The Gadget-2 SPH equations are presented here, with emphasis on the necessity for including extra, purely numerical terms in the implementation of the continuum equations above. For further details, we refer the reader to much more comprehensive discussions elsewhere, e.g. (Monaghan 2005; Price 2010).

The fluid is taken to have a polytropic equation of state (EOS),

$$P = K(s)\rho^\gamma = (\gamma - 1)\rho\epsilon, \quad (4)$$

where  $s$  is the specific entropy. Following standard usage (e.g., Landau & Lifshitz (1959)), a polytropic gas is defined as having constant specific heats, and therefore the related adiabatic index,  $\gamma$ , is constant. While some authors restrict  $K$  to being constant as well (and refer to it as the polytropic constant), here it is allowed to vary, and in the following  $K$  is referred to as the entropic function. In Gadget-2, this  $K$  is evolved rather than  $\epsilon$ , giving the strict conservation properties of both energy and entropy mentioned above (Springel & Hernquist 2002). In the following, the subscripts  $\{a, b\}$  will be used only to distinguish individual fluid elements, represented in SPH as finite volume pseudo-particles, and not to signify vector components.

First, the mass density at the location of a given particle labelled as ‘ $a$ ’ and with spatial coordinate vector,  $\mathbf{r}_a$ , is calculated at each timestep by direct summation using

$$\rho_a = \sum_b^{N_n} m_b W_a. \quad (5)$$

The summation is performed over  $N_n$  ‘nearest neighbour’ particles labelled as ‘ $b$ ’ (typically  $\approx 50$  (Navarro & White 1993)), each with mass,  $m_b$ , and contained within a radius given by the smoothing length,  $h_a$ . The kernel,  $W_a = W(|\mathbf{r}_{ab}|, h_a)$ , is strongly peaked and differentiable (a cubic spline, in Gadget-2) and with  $|\mathbf{r}_{ab}| = |\mathbf{r}_a - \mathbf{r}_b| < h_a$ . The smoothing length is calculated at each timestep such that the kernel volume of a particle contains a constant mass (for numerical stability), according to the following relation:

$$\frac{4\pi}{3} h_a^3 \rho_a = N_n \bar{m} = \text{const.}, \quad (6)$$

where  $\bar{m}$  is the average particle mass. Within the fluid, the resolution is essentially determined by the magnitude of  $h_a$ , over which discontinuities are smoothed.

To evolve the particle velocity, the non-viscous Euler equation, including a gravitational potential,  $\phi$ , is represented as:

$$\left( \frac{d\mathbf{v}_a}{dt} \right)_{\text{nv}} = - \sum_b^{N_n} m_b \left( f_b \frac{P_b}{\rho_b^2} \nabla W_b + f_a \frac{P_a}{\rho_a^2} \nabla W_a \right) + \nabla \phi_a, \quad (7)$$

where

$$f_a = \left( 1 + \frac{h_a}{3\rho_a} \frac{\partial \rho_a}{\partial h_a} \right)^{-1}. \quad (8)$$

The factors,  $f_a$ , arise from the Lagrangian derivation and the set of constraints on coordinates provided by Eq. 6; they account directly for the variation in smoothing lengths in the system (Springel & Hernquist 2002). Self-gravity among particles is calculated efficiently using a tree algorithm (a hierarchical multipole expansion) (Barnes & Hut 1986). Additionally, in some cases we include the acceleration due to a (Newtonian) central object located at the origin of the simulation’s coordinates,  $\nabla \phi_a = -GM_C \hat{\mathbf{r}}_a / r_a^2$ .

Gadget-2 uses an artificial viscosity of the form

$$\Pi_{ab} = \begin{cases} -\alpha_v (\bar{c}_{ab} w_{ab} - 3w_{ab}^2) / 2\bar{\rho}_{ab} & \text{for } \mathbf{v}_{ab} \cdot \mathbf{r}_{ab} < 0, \\ 0 & \text{for } \mathbf{v}_{ab} \cdot \mathbf{r}_{ab} \geq 0, \end{cases} \quad (9)$$

with  $\mathbf{v}_{ab} = \mathbf{v}_a - \mathbf{v}_b$  and  $w_{ab} = (\mathbf{v}_{ab} \cdot \mathbf{r}_{ab}) / |\mathbf{r}_{ab}|$  being the relative velocity between particles in vector and scalar form, respectively;  $\bar{\rho}_{ab} = (\rho_a + \rho_b) / 2$ , the average density;  $c_a = (\gamma P_a / \rho_a)^{1/2}$ , the local soundspeed, with average  $\bar{c}_{ab} = (c_a + c_b) / 2$ ; and  $\alpha_v \approx 1$ , a free parameter for the strength of the viscosity. In practice,  $\Pi_{ab}$  acts similarly to a pressure term in the Euler equation, and the related acceleration is:

$$\left( \frac{d\mathbf{v}_a}{dt} \right)_{\text{v}} = - \sum_b^{N_n} m_b \Pi_{ab} \nabla \bar{W}_{ab}, \quad (10)$$

where  $\bar{W}_{ab} = (W_a + W_b) / 2$ .

The  $\Pi_{ab}$  formulation possesses two terms to mimic naturally-occurring, dissipative processes. The first (linear in  $w_{ab}$ ) provides both the bulk and shear viscosity of the converging particles, and the second (quadratic in  $w_{ab}$ ) functions as a von Neumann-Richtmyer artificial viscosity for shock handling and for spreading shock discontinuities over the smoothing length of supersonic particles. The quadratic term also prevents interparticle penetration. It should be noted that this single artificial viscosity provides both shear and bulk viscosities, which would be given by separate terms in the physical, Navier-Stokes description (direct implementations of the latter are discussed briefly below). In many SPH prescriptions the linear and quadratic terms are scaled by separate free parameters,  $\alpha_v$  and  $\beta_v$ , respectively, each with a range of ‘typical’ values, but we here follow the practice of setting  $\beta = 3\alpha$  (unless otherwise stated). An in-depth discussion of the relative scaling of the linear and quadratic terms is provided by (Monaghan 1997).

The entropic function,  $K$  (defined in Eq. 4), changes, in general, in the presence of viscosity:

$$\frac{dK_a}{dt} = \frac{1}{2} \left( \frac{\gamma - 1}{\rho_a^{\gamma-1}} \right) \sum_b^{N_n} m_b \Pi_{ab} \mathbf{v}_{ab} \cdot \nabla \bar{W}_{ab}. \quad (11)$$

Cooling in optically thin material may be included in a straightforward manner by subtracting the appropriate entropy loss at the end of a timestep. The inclusion of accurate radiative transport in optically thick material is a separate (and highly non-trivial) task, which we do not consider here.

Finally, to limit spurious angular momentum transfer which arises in shear flow due to the form of the artificial viscosity, the simple Balsara correction is commonly utilised (Balsara 1995; Steinmetz 1996). The aim of this factor is to

remove the effect of the artificial viscosity when there is a pure shearing motion and to have it acting only when there is a compression. An estimate of the relative amount of local shear is made from the curl and divergence of the particle velocities:

$$g_a = \frac{|\nabla \cdot \mathbf{v}|_a}{|\nabla \times \mathbf{v}|_a + |\nabla \cdot \mathbf{v}|_a + (0.0001 c_s/h_a)}, \quad (12)$$

where the third term in the denominator prevents the quantity from diverging. The average value of this quantity for two interacting particles is used as a multiplicative factor in front of  $\Pi_{ab}$ , producing the modified form  $\Pi'_{ab} = \Pi_{ab} (g_a + g_b)/2$ , which is then used instead of  $\Pi_{ab}$  in Eqs. 10 and 11. In the following, we examine the effect of the artificial viscosity both with and without the Balsara correction (the former case being the default).

Eqs. 5, 7 and 11, together with the EOS and the smoothing length condition in Eq. 6, form a complete set of equations for evolving the physical, hydrodynamic quantities in numerical simulations. However, as part of the process of discretisation, a number of additional variables and parameters have been included ( $h$ ,  $W$ , etc.). While these are used to model realistic properties of the discretised system, such as continuity and shocks, they also introduce purely numerical features by controlling resolution, the ‘spread’ of shocks and the stability of interpolations and summations. In the past decades, much work has been done to determine reliable values and forms for these parameters and to reduce associated numerical artefacts. Generally, a number of standard problems, in various dimensions and geometries, are used to test the behaviour of a given code and the associated parameters.

Another purely numerical consideration in using SPH is the initial placement of the particles representing points in the flow (Imaeda & Inutsuka 2002; Monaghan 2006). For instance, regularities in particle configurations may lead to the propagation of artificial structures in the simulation along preferred directions, and even randomised placements may produce numerical features, e.g., due to local overdensities. For each simulation presented here, the initial particle setup was created using an algorithm which maps a non-regular but constant number density profile of (equal-mass) particles into the arbitrary number-density (and trivially, mass-density) profile of the desired model. This method has also been applied in other simulations (Taylor, Miller & Podsiadlowski 2011) and is described in Appendix A.

### 3 EXISTING (KINEMATIC) APPROXIMATIONS OF $\nu$

The standard ring-spreading test starts from an initial  $\delta$ -function ring of matter in circular Keplerian motion around a gravitating point mass (Lüst 1952; Lynden-Bell & Pringle 1974). If shear viscosity is present, this ring will proceed to spread out into a disc, with the rate of spreading dependent on the magnitude of the viscosity. The matter is taken here to behave isothermally, with the temperature and viscosity being sufficiently small so that the spreading is slow and the thin disc is essentially Keplerian (with its height,  $H$ , being small compared with the radial coordinate,  $r$ , at any

point) (Pringle 1981). With certain additional simplifying assumptions (negligible self-gravity for the disc material and constant viscosity coefficient,  $\nu$ ), an analytic solution can be obtained for the ring-spreading (Flebbe et al. 1994; Murray 1996; Speith & Riffert 1999).

The exact analytic results provide a means for comparison for an SPH simulation of an equivalent configuration with no viscosity apart from that of the numerical scheme,  $\nu_{\text{SPH}}$ . From the analytic results, an effective value for the shear component of the artificial viscosity can then be estimated, if one assumes that  $\nu_{\text{SPH}}$  is roughly constant throughout the disc (a somewhat doubtful assumption) and that the corresponding bulk component has negligible effect (a very good assumption under the circumstances envisaged). The value obtained can then be translated into an effective Shakura-Sunyaev  $\alpha$  coefficient [25], which represents the viscosity according to

$$\nu = \alpha c_s H, \quad (13)$$

where  $H$  is the disc height, and  $c_s$  is the sound speed.

The analytic solution gives an expression for the surface density of the ring,  $\Sigma_{\text{R}}$ , as a function of position and time. For the conditions mentioned above, the radial velocity  $v_r$  (positive for ‘outer’ material and negative for ‘inner’ material) is always small, with  $v_r \sim \nu/r \ll v_\phi$  by scaling arguments (Frank, King & Raine 2002). The surface density is then given by

$$\Sigma_{\text{R}}(r, \tau) = \frac{M_{\text{D}}}{\pi \tau r^{1/4}} \exp\left(\frac{-1 - r^2}{\tau}\right) I_{1/4}\left(\frac{2r}{\tau}\right), \quad (14)$$

where  $r$  is the radius in the equatorial plane (with  $r = 1$  initially);  $\tau$  is a time parameter ( $\tau = 12\nu t$ );  $\nu$  is the kinematic shear viscosity coefficient;  $M_{\text{D}}$  is the disc mass (taken as the mass unit, i.e.  $M_{\text{D}} = 1$ ), and  $I_{1/4}$  is a modified Bessel function. A detailed derivation of this formula is given by, e.g., Frank, King & Raine (2002).

In our work reported below, the corresponding numerical simulations begin a short time after the axisymmetric ring has spread to a finite thickness (at  $\tau_0 = 0.01$ ) using the analytic formula Eq. 14 to provide the initial surface density profile. This same formula is also used for matching against the simulation properties at subsequent times (doing so has been justified in previous numerical studies by the general proximity of the surface density evolution to this expression). Self-gravity of the SPH particles is included in simulations, although it is assumed that the acceleration due to the central point mass dominates (we take  $M_{\text{C}}/M_{\text{D}} = 1000$ ). SPH particles are removed from the system at an inner boundary with small radius,  $r = 0.1$ .

As mentioned above, in addition to the ring-spreading test there are also some approximate analytic formulations for estimating the effective shear viscosity of the disc from kinematic considerations: that of Murray (1996) is

$$\nu_{\text{M}} = \alpha_{\text{v}} c_s h / 16, \quad (15)$$

while that of Lodato & Price (2010) is

$$\nu_{\text{LP}} = \alpha_{\text{v}} c_s h / 20. \quad (16)$$

These relations are generated essentially by reversing the summation form of SPH equations which involve artificial viscosity back to continuum limits. Further details are given

in the respective papers. Note that the Gadget-2 definition of smoothing length has been used in each case.

## 4 ESTIMATING LOCAL $\nu$ FROM ENTROPY OR VISCOUS ENERGY PRODUCTION

### 4.1 Motivation from fluid equations

An artificial viscosity term ( $\propto \Pi_{ab}$ ) appears in both the momentum and energy hydrodynamic equations. Each of these roles affects the evolution and structure of the system, as the trajectories of fluid elements are modified and as kinetic energy is transformed into heat. The standard form of the (isothermal) ring-spreading test has been used essentially to analyse the effective viscosity via the Euler equation, with the spreading being caused by the combined action of the viscous and several other additive terms<sup>1</sup>, but it seems better to use, instead, the energy equation, where the effect of viscosity in generating entropy can be clearly singled out.

Internal energy in fluid systems can be produced both by viscosity and by non-viscous compression. This is expressed in the first law of thermodynamics, as applied to a co-moving fluid element with unit mass:

$$d\epsilon = T ds - P d(1/\rho), \quad (17)$$

where  $T$  is the temperature and  $s$  is the specific entropy. The specific internal energy produced by viscosity,  $d\epsilon_v$ , corresponds to the first term on the right hand side, and its time derivative is simply

$$\dot{\epsilon}_v \equiv T \dot{s}. \quad (18)$$

This quantity can be calculated directly from the SPH expressions in all cases, whatever the flow geometry or equation of state, giving a direct local measure of the effects of viscosity. The only caveat is that there should be no other sources of entropy production to contaminate the interpretation.

For the particular case of the (widely used) class of polytropic equations of state implemented by Gadget-2, the derivative of Eq. 4 gives the following expression for  $d\epsilon$ :

$$\begin{aligned} d\epsilon &= \frac{\rho^{\gamma-1}}{\gamma-1} dK + K \rho^{\gamma-2} d\rho, \\ &= \frac{\rho^{\gamma-1}}{\gamma-1} dK - P d\left(\frac{1}{\rho}\right), \end{aligned} \quad (19)$$

where the relations  $P = K\rho^\gamma$  and  $d(1/\rho) = -d\rho/\rho^2$  have been used in arriving at the form of the second line. Matching terms with the first law in Eq. 17 and referring to Eq. 18 leads to the following set of formulae linking  $\dot{K}$ ,  $\dot{s}$  and  $\dot{\epsilon}_v$ :

$$\dot{K} = \frac{(\gamma-1)T}{\rho^{\gamma-1}} \dot{s} = \frac{(\gamma-1)}{\rho^{\gamma-1}} \dot{\epsilon}_v. \quad (20)$$

Within Gadget-2, computation of the evolution of  $\epsilon_v$  is very similar to that for the entropic function,  $K$  (cf. Eqs. 11, 18 and 20):

<sup>1</sup> In practice, ring-spreading is performed in 2D only, with the thermal pressure terms zeroed in a ‘cold’ disc approximation to isolate the viscous term, so that the 3D behaviour of the artificial viscosity is typically not measured.

$$\frac{d\epsilon_{va}}{dt} = \left( \frac{\rho_a^{\gamma-1}}{\gamma-1} \right) \frac{dK_a}{dt} = \frac{1}{2} \sum_b^{N_n} m_b \Pi_{ab} \mathbf{v}_{ab} \cdot \nabla \bar{W}_{ab}, \quad (21)$$

and this can be evaluated straightforwardly for each fluid element. Note that in the further specialisation to an isothermal equation of state with  $\gamma = 1$  (which we will be using below for making comparison with the ring-spreading test), then the entropic function,  $K$ , becomes a constant, but the true entropy,  $s$ , continues to change under the action of viscosity, as does  $\epsilon_v$ .

Importantly,  $\dot{\epsilon}_v$  is determined from the contribution of only a single term which contains  $\Pi_{ab}$ . In quantifying the effect of any SPH artificial viscosity prescription on a disc system, this isolation greatly simplifies analysis (and interpretation). In general, entropy can be produced by shearing, normal compression and shock compression, the totality of which are accounted for when measuring  $\dot{\epsilon}_v$ , due to its general relation to specific entropy. In contrast, only the shearing is important under the assumptions of the ring-spreading test (or the analytic approximations).

### 4.2 Local viscous heating of fluid elements

Monitoring  $\dot{\epsilon}_v$  already provides a suitable way of demonstrating the local effects of artificial viscosity, and one could stop at that point. However, if one wants to calculate an effective shear viscosity coefficient (for circumstances involving shear and no significant compression), one needs to write an expression for  $\dot{\epsilon}_v$  in terms of  $\nu$  and the shearing velocity field (see, e.g., Appendix B of Tassoul (1978)) and then to invert it to give an expression for  $\nu$ . For general planar rotational motion, one finds the following expression for specific internal energy creation (Szuszkiewicz & Miller 1997):

$$\dot{\epsilon}_v = \frac{4}{3} \nu \left[ \left( \frac{\partial v_r}{\partial r} \right)^2 + \frac{v_r^2}{r^2} - \frac{\partial v_r}{\partial r} \frac{v_r}{r} \right] + \nu \left( r \frac{\partial \Omega}{\partial r} \right)^2, \quad (22)$$

using cylindrical polar coordinates  $(r, \phi, z)$  here and after. This form may be inverted easily for an expression of the effective viscosity:

$$\nu(r) = \frac{3\dot{\epsilon}_v}{4} \left[ \left( \frac{\partial v_r}{\partial r} \right)^2 + \frac{v_r^2}{r^2} - \frac{\partial v_r}{\partial r} \frac{v_r}{r} + \frac{3}{4} \left( r \frac{\partial \Omega}{\partial r} \right)^2 \right]^{-1}. \quad (23)$$

Each term on the right hand side is composed of variables which are directly obtainable from the SPH particles. As discussed above, the viscous heating is a direct measure of entropy creation due to viscosity, and the gradient terms may be estimated, e.g., within SPH particle kernels or from averaged ring values.

In this study, we describe and utilise an expression which includes solely the term involving  $\Omega$ . This facilitates comparisons with existing approximations and, as shown below, leads to particularly simple expressions of  $\nu(r)$  (though, it must be emphasised, that the preceding expression is by no means prohibitively complicated).

The surface area of a narrow, axisymmetric ring of width,  $\Delta r$  (centred around  $r$ ), is  $2\pi r \Delta r$ , and the mass of the ring is therefore  $\Delta m = 2\pi r \Sigma \Delta r$ . Taking the matter to be moving on basically circular orbits, the viscous torque exerted on the ring can be written as (Frank, King & Raine 2002):

$$G(r) = \frac{d\Omega}{dr} 2\pi r^3 \nu \Sigma. \quad (24)$$

The work done by this torque leads to local heating in the rotating flow. The specific heating rate due to viscosity is

$$\begin{aligned} \dot{\epsilon}_v(r) &= \frac{d\Omega}{dr} \frac{G(r)}{\Delta m} \frac{\Delta r}{\Delta m} = \left( \frac{d\Omega}{dr} \right)^2 \frac{2\pi r^3 \nu \Sigma \Delta r}{\Delta m}, \\ &= \nu \left( r \frac{d\Omega}{dr} \right)^2, \end{aligned} \quad (25)$$

which is recognized as the final term in Eq. 22.

After trivial rearrangement, the expression for the viscosity is given in terms of easily known quantities as:

$$\nu(r) = \left( r \frac{d\Omega}{dr} \right)^{-2} \dot{\epsilon}_v. \quad (26)$$

Compared to existing methods for evaluating effective viscosity in rotating flows, this expression is particularly general, having made no assumptions of rotation profile, equation of state, constancy of  $\nu$  or artificial viscosity prescription. Moreover, as a function of radius, this expression provides a more detailed and useful description of viscous behaviour throughout the simulation. As noted above, more general viscous stresses may be applied as well, such as that of Eq. 22. In the following examples, we implement Eq. 26 with different disc structures and using different artificial viscosity prescriptions.

## 5 EXAMPLES AND COMPARISONS

### 5.1 Local heating applied to thin discs

In the examples below, we apply the expression for the effective local viscosity in Eq. 26 to test scenarios of ring-spreading and thin disc cases. Using assumptions of axisymmetry and circular, Keplerian orbits, the viscosity expression is

$$\nu(r) = \frac{4}{9} \frac{\dot{\epsilon}_v}{\Omega_K^2}. \quad (27)$$

Presuming vertical equilibrium with some thin disc scale height,  $H$ , the Shakura-Sunyaev  $\alpha$  is then given as

$$\alpha(r) = \frac{4}{9} \frac{\dot{\epsilon}_v}{\Omega_K^2 c_s H}. \quad (28)$$

In the case of polytropic, nonisothermal equations of state, these expressions for viscosity and the Shakura-Sunyaev  $\alpha$  may be written in terms of the entropic function as:

$$\nu(r) = \frac{4}{9} \frac{\rho^{\gamma-1} \dot{K}}{(\gamma-1) \Omega_K^2}, \quad (29)$$

$$\alpha(r) = \frac{4}{9} \frac{\rho^{\gamma-1} \dot{K}}{(\gamma-1) \Omega_K^2 c_s H}, \quad (30)$$

respectively. These last forms are particularly relevant to Gadget-2, where the entropic function is directly evolved, and they are used in obtaining the results presented below.

Finally, it is interesting to note that, for the specific case of an isothermal EOS, Eq. 28 may be expressed neatly as:

$$\alpha(r) = \frac{4}{9} \frac{\dot{\epsilon}_v}{\Omega_K c_s^2} \propto \frac{t_{\text{dyn}}}{t_{\text{th},v}}, \quad (31)$$

using the expression for the scale height given in Eq. 32, below. Physically, in this latter form,  $\alpha$  directly relates the local dynamical timescale ( $t_{\text{dyn}} = \Omega^{-1}$ ) and the viscous thermal timescale ( $t_{\text{th},v} \propto c_s^2 / \dot{\epsilon}_v$ ), as it should from accretion disc theory (e.g., Pringle (1981)).

### 5.2 Thin Disc Structure

We now briefly describe the structure equations for the two varieties of thin isothermal discs used in this study (in dimensionless units). Each disc is taken to be in vertical, hydrostatic equilibrium with respect to the gradient of the gravitational potential of the massive central object. The density distribution, scale height and central density (in the equatorial plane) are, respectively:

$$\begin{aligned} \rho(r, z) &= \rho_c(r) \exp \left[ -\frac{1}{2} \left( \frac{z}{H(r)} \right)^2 \right], \\ H(r) &= \left[ \frac{r^3 c_s^2}{GM_C} \right]^{1/2} = \frac{c_s}{\Omega_K}, \\ \rho_c(r) &= \frac{\Sigma(r)}{[2\pi]^{1/2} H(r)}. \end{aligned} \quad (32)$$

Since this Gaussian density profile only asymptotically approaches zero in the vertical direction, an arbitrary disc height for the boundary of SPH particles above/below the equatorial plane at any radius must be designated, and we set this to be three times the scale height in order to incorporate > 99% of the mass of the theoretical distribution into the simulation (though, the non-arbitrary scale height,  $H$ , is used everywhere else in the analytic relations and discussion).

The vertical velocity is taken to be uniformly zero, and the profile of the azimuthal velocity is very nearly Keplerian, i.e.,  $v_\phi(r, z) \approx v_K(r)$ . The global sound speed,  $c_s$ , is a parameter restricted in accordance with the thinness condition,  $H \ll r \Rightarrow c_s^2 \ll GM_C/r$ , or  $v_K^2/c_s^2 \equiv \mu^2 \gg 1$ , where  $\mu$  is essentially the Mach number of the (very supersonic) azimuthal flow. Using both the height from Eq. 32 and the definition of the viscosity parametrisation in Eq. 13, the global disc viscosity can be related to the Shakura-Sunyaev  $\alpha$  as a function of  $\mu$  and the Keplerian specific angular momentum,  $j_K$ :

$$\nu = \alpha \frac{r v_K}{\mu^2} = \alpha \frac{j_K}{\mu^2}. \quad (33)$$

Finally, the initial surface density of the flows must be supplied for use in Eqs. 32. The formulation of the spreading ring,  $\Sigma_R$ , has been given in Eq. 14. We have also calculated a more disc-like system (of similar mass and surface density), with radial span at  $t = 0$  of  $(r_{\text{min}}, r_{\text{max}}) = (0.7, 1.4)$ . Here, the arbitrary surface density profile has been chosen to be flat in this region initially,  $\Sigma_F(r, 0) = \Sigma_R(1, \tau = 0.01)/2$ , and the resulting disc mass was  $\approx 2$ . This is considered solely as a separate test case and not as a representation of a specific, physical system (e.g., the initial boundaries are too discontinuous for an equilibrium system).

### 5.3 Global and local viscosity estimates

Here, we first present results for ring-spreading tests with the Balsara correction included for various values of the

**Table 1.** Comparison of viscosity parameter values at multiple resolutions, from both local (entropic) and global (kinematic) methods for the same disc ( $\mu_1 = 30$ ) shown in Fig. 1 (at  $t = 2000$ ).

parameter	method	$N = 5 \times 10^4$	$1 \times 10^5$	$2 \times 10^5$
$h_{\text{ave}}$	-	0.058	0.045	0.036
$\nu_{\text{ave}}/(10^{-6})$	entr.	6.0	4.6	3.5
$\nu_{\Sigma, \text{m}}/(10^{-6})$	entr.	4.9	3.7	2.7
$\nu/(10^{-6})$	kin.	3.5	2.6	2.1
$\alpha_{\text{ave}}$	entr.	0.056	0.042	0.032
$\alpha_{\Sigma, \text{m}}$	entr.	0.046	0.035	0.026
$\alpha$	kin.	0.03	0.02	0.02

parameter,  $\mu_1 \equiv \mu(r = 1)$ , where  $r = 1$  is the radius of the initial midpoint of the ring (and using units in which  $GM_C = 0.01$ ). First, the viscous properties are determined kinematically by using the global evolution of the surface density and fits to the theoretical progression given by the analytic formulation. Then, local values of  $\nu$  and  $\alpha$  are calculated from  $\dot{\epsilon}_v$  using Eqs. 27-28. Unless stated otherwise,  $\alpha_v = 0.8$  in all of the presented simulations (and, in the notation of §2, the quadratic term coefficient,  $\beta_v = 2.4$ ).

The top panel of Fig. 1 shows the  $\Sigma_R$  time evolution of a ring with  $\mu_1 = 30$  at a resolution of  $N = 5 \times 10^4$  (binned values plotted as diamonds). The value of  $\nu = 3.5 \times 10^{-6}$  can then be inferred by matching with analytic fits given by Eq. 14, which are also shown (solid lines). Use of Eq. 33 then easily yields values of  $\alpha \approx 0.03$  at  $r \approx 1$ . The profile from the simulation roughly matches the analytic expectation, and while fitting the curves, more weight was given to the locations of peak surface density, with the inner and outer margins being slightly over- and under-dense, respectively. It is striking that there is non-negligible effective shear viscosity present in these simulations, even with the Balsara correction.

The local estimates of viscosity parameters coming from measuring  $\dot{K}$  and evaluating Eqs. 27-28 are also shown in Fig. 1, where  $\nu_{\text{ave}}$  is a mass-weighted average between  $0.5 \leq r \leq 1.5$ , and  $\nu_{\Sigma, \text{m}}$  is the value for the annulus with maximum surface density (same notations for  $\alpha$ ). For a given flow, both sets of locally-estimated values of kinematic viscosity and Shakura-Sunyaev  $\alpha$  are roughly similar to the globally-obtained curve-fits, though always having larger magnitudes. Comparing the results of the two methods, the values at the peak surface density of the local calculations are much closer to those of the global estimates, which is not surprising given that the former emphasised the maximum-density regions in fitting. Results from higher resolution rings were similar but showed a slight resolution dependence in the effective viscosity values obtained (discussed further below); a comparison of parameters is given in Table 1.

The profiles of the local  $\nu$  and  $\alpha$  values (lower two panels of Fig. 1) are roughly constant with time (and also for the various resolutions tested), with minima near the location of maximal  $\Sigma_R$ . This can be understood by examining the corresponding heating rate profiles in Fig. 2. In the expanding layers at  $r > 1$ ,  $\dot{\epsilon}_v$  is nearly constant, and therefore, by Eq. 27,  $\nu \propto r^3$ . The inner layers are compressed as they spread and have a much higher heating rate. In the

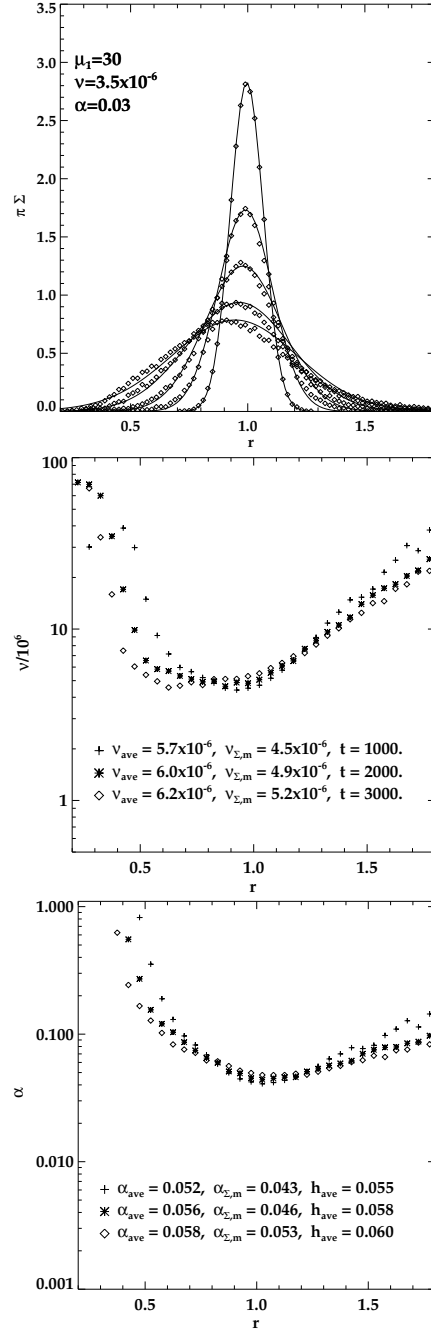


**Figure 1.** (Here and following:) Top: standard  $\nu$  and  $\alpha$  estimation from  $\Sigma_R$  evolution ( $\diamond$ ) with analytic solution (solid line), shown at  $t = 0, 400, 1000, 2000$  and  $3000$ . Middle: local  $\nu$  (average and value at maximum  $\Sigma$ ) from Eq. 27. Bottom: local  $\alpha$  from  $\nu$  values in middle panel, using Eq. 28, and average smoothing length,  $h_{\text{ave}}$ .  $N=50k$ .

regions containing the most mass ( $0.7 \leq r \leq 1.3$ ), the values of viscosity and the Shakura-Sunyaev parameter are fairly constant, in accord with the overall model assumptions.

The large viscosity values at the inner and outer disc boundaries (Fig. 1) correspond to very low density regions which are poorly resolved. A consequence of the smoothing length condition in Eq. 6, used to stabilise the interpolations, is that particle kernels are artificially large at the edges of the simulation, and therefore the density is artificially low.

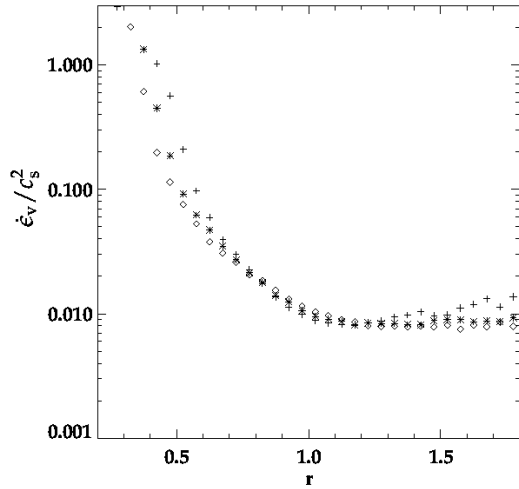


**Figure 2.** The (scaled) specific heating,  $\dot{\epsilon}_v/c_s^2$ , at  $t = 1000$  ('+'), 2000 ('\*') and 3000 ('o') from the same simulation shown in Fig. 1. The heating is mostly constant for the ‘outflowing’ material at  $r > 1.0$  but is much higher for inner radii.

Hence, Gadget-2 and other SPH formulations with similarly defined smoothing lengths necessarily require careful boundary conditions. As a function of time, the values of both  $\alpha_{\text{ave}}$  and  $\alpha_{\Sigma, \text{m}}$ , increase slightly (along with  $h_{\text{ave}}$ ).

Fig. 3 shows results from investigating other values of  $\mu_1$  ( $= 60$  and  $120$ ), again using  $5 \times 10^4$  particles. For both the global/kinematic and local/entropic measures,  $\alpha$  increases with increasing  $\mu_1$ , whereas  $\nu$  decreases (with the local/entropic values being systematically higher than the global/kinematic ones in each case). The resolution trends are the same as those for  $\mu_1 = 30$ . It then appears that, while the value of the artificial viscosity parameter has remained constant ( $\alpha_v = 0.8$  for all of these simulations), the kinematic viscosity and disc- $\alpha$  depend on both the sound speed and the resolution. To explain the former dependence, one can note that  $c_s$  appears directly in the expression for  $\Pi_{ab}$  in Eq. 9. The latter dependence results from the fact that, inherently in SPH, the smoothing length of a fluid element determines the length scale of its interactions. With decreasing particle number, the cross-sectional spread of an element increases ( $h_{\text{ave}}^2 \propto N^{2/3}$ ), resulting in greater shear in the flows. Using only the bulk term in  $\Pi_{ab}$  for studying non-axisymmetric discs, (Murray 1996) estimated linear dependence for both sound speed and smoothing length (which was assumed to be constant), i.e.,  $\nu \propto c_s h$ ; recently similar analysis has been performed for the case of artificial tensor-viscosity in studies of warped discs by (Lodato & Price 2010).

This dependency of effective viscosity on features which vary across the disc shows the importance of local measurement. Both the spatial and temporal variations in surface density away from the exact analytic solution have been noted above. In using the local estimates to determine parameters with Eqs. 27-28, one has the dual advantage of avoiding any arbitrariness which arises in global curve-fitting and of characterising radial dependences quantitatively. This approach allows a more complete description of the behaviour of the SPH artificial viscosity in the ring.

For example, in the very thin  $\mu_1 = 120$  rings the effec-

tive viscosity has a much smaller constant-value region than in rings with higher  $c_s$ . Profiles of  $\alpha$  steeply increase to either side of  $r \approx 1$ , also making analytic curve-fitting less exact. Apart from differences due to compression and expansion of annuli, the curves reflect the influence of boundary conditions and the effectively poorer resolution within these flattened discs ( $H \propto \mu^{-1}$ ), even though the volume is smaller for the same  $N$ : since the ratio of surface area to volume is necessarily larger as well, the kernels of more SPH particles encompass empty space outside the disc, artificially increasing  $h$  (and similarly decreasing  $\rho$ ). This would suggest the practical necessity for increased  $N$  in thinner, high- $\mu$  discs to avoid numerical effects in the viscous evolution and artificially high accretion rates. In some sense, this is a statement of the intuitive notion that a resolution criterion such as  $H/h \geq$  (a few) is required for accurately characterizing discs.

As a comparison, we now investigate rotating flows with flatter surface density profiles, for which the ‘empty kernel’ boundary behaviour should have less effect on the evolving system. We therefore use local viscosity measures to analyse the systems with the  $\Sigma_{\text{F}}$  defined in §5.2, which are initially more ‘disc-like’ in the sense of having a greater radial extent of mass. Time-evolution profiles of surface density are shown in Fig. 4 for  $\mu_1 = 60$  and  $\mu_1 = 120$ . Indeed, for these discs the values of  $\nu$  and  $\alpha$  are fairly constant functions of radius, and, for a given  $\mu_1$ , the measured viscosity values agree well with those from the ring tests.

In order to quantify the behaviour of the Balsara-corrected artificial viscosity prescription,  $\Pi'_{ab}$  with a given  $\alpha_v$ , for rotating flows with different resolutions and sound speeds, the resulting Shakura-Sunyaev parameter values for all rings and discs from this study were plotted in  $h_{\text{ave}}-\alpha_{\text{ave}}$  and  $h_{\text{ave}}-\alpha_{\Sigma, \text{m}}$  planes (Fig. 5). Note that the  $\alpha$  values appear to vary quite linearly with smoothing length, with  $\mu_1$  determining the gradient; the values of  $\alpha_{\Sigma, \text{m}}$  appear to be independent of the specific profile of surface density, whereas disc values have noticeably lower values of  $\alpha_{\text{ave}}$  than the rings. This (small) qualitative difference is to be expected, as boundaries affect the former less. While the values in both plots appear to be quasi-convergent towards  $\alpha = 0$  as  $h_{\text{ave}}$  tends to zero, it is not possible to be precise about this due to the approximate nature of the plot.

## 5.4 Further examples and altering artificial viscosity

### 5.4.1 Evaluating the artificial viscosity in Balsara-corrected flows

The simulations presented above have all utilised the same value of  $\alpha_v = 0.8$  and the Balsara-corrected form for the artificial viscosity,  $\Pi'_{ab}$ . In this section we investigate the effects of varying  $\alpha_v$ , using only the local entropy production method to measure the viscous properties of the flows. It should be noted that for these predominantly smooth and non-shocking flows, the linear term of the artificial viscosity dominates entropy production. Neglecting the quadratic term ( $\beta_v = 0$ ) produces very little change in the disc flow. Therefore, we only further consider here the effects of varying  $\alpha_v$  and of using or not using the Balsara correction.

With  $\Pi'_{ab}$ , even significantly different values of  $\alpha_v$  result



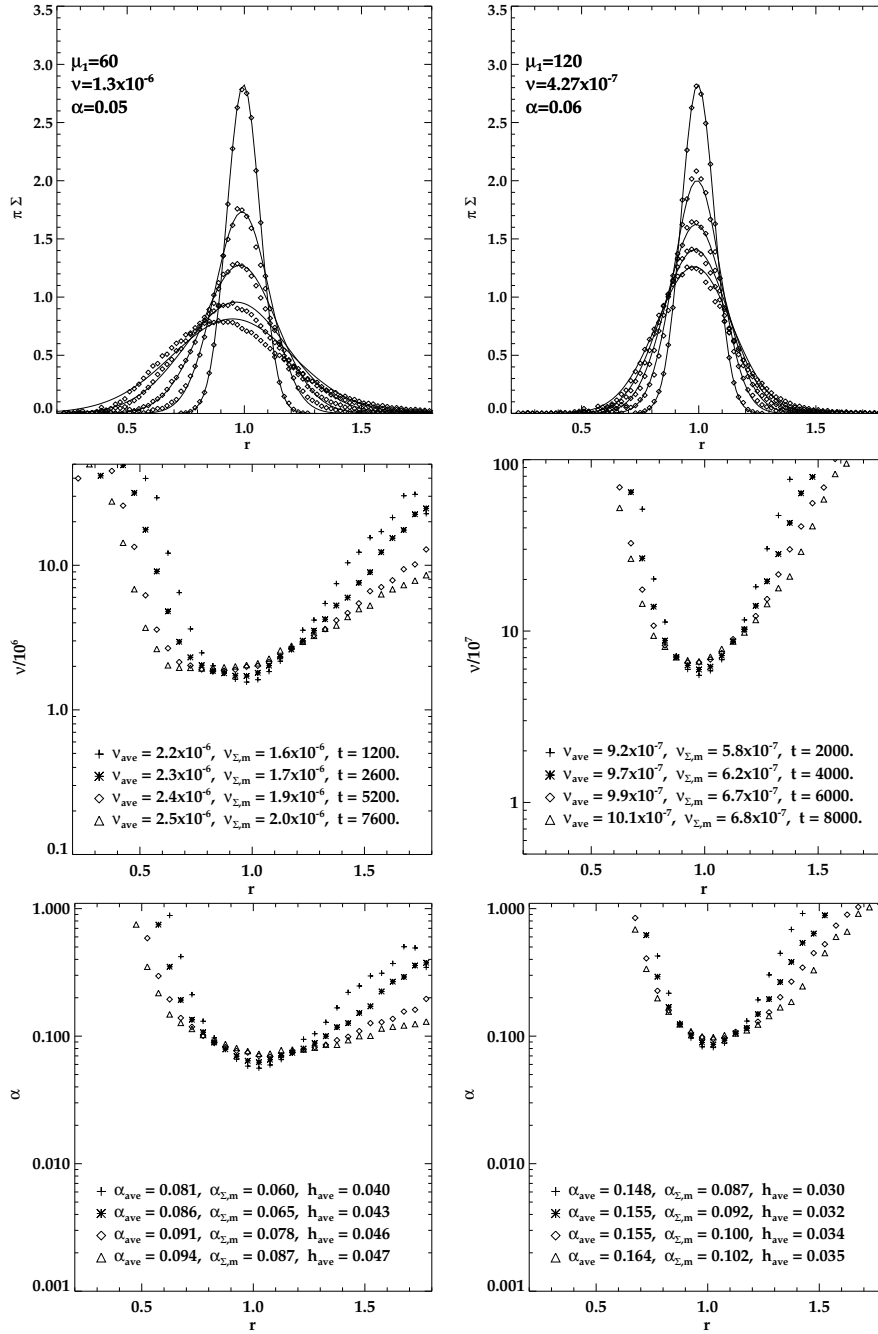


**Figure 3.** Ring-spreading test with  $N=50k$ , shown at times given in the middle panel (and at  $t = 0$ , top). Left,  $\mu_1 = 60$ ; right,  $\mu_1 = 120$  (cf. Fig. 1 for notations).

in only minor changes of the disc parameters, as was to be expected. Originally, the ring with  $\mu_1 = 30$  and  $\alpha_v = 0.8$  (seen in Fig. 1) had  $(\alpha_{ave}, \alpha_{\Sigma,m})$  values of approximately (0.056, 0.046); increasing to large values of  $\alpha_v = 1.6$  and 2.4 resulted in (0.060, 0.049) and (0.066, 0.057), respectively; only at extremely high values were significant changes seen, e.g.  $\alpha_v = 8.0$  yielded (0.109, 0.091). Thus, in these purely rotational flows, the shear-correction does limit the artificial viscosity term (although we stress again that it remains significantly non-zero), and the values shown in Fig. 5 are roughly independent of  $\alpha_v$  within the range studied. From fitting various disc parameters for results from the preced-

ing simulations (across a range of radii,  $0.5 < r < 1.5$ ), it emerges that the effective viscosity is well represented by the following (simple) expression:

$$\alpha(r) \approx \frac{1}{16} \left[ \frac{h(r)}{2H(r)} \right], \quad (34)$$

explicitly noting that  $\alpha$  generally varies with position, as both the smoothing length and disc height are functions of radius. Therefore, when the Balsara correction is applied, the interaction length among particles appears to strongly determine the viscous dissipation in the flow.

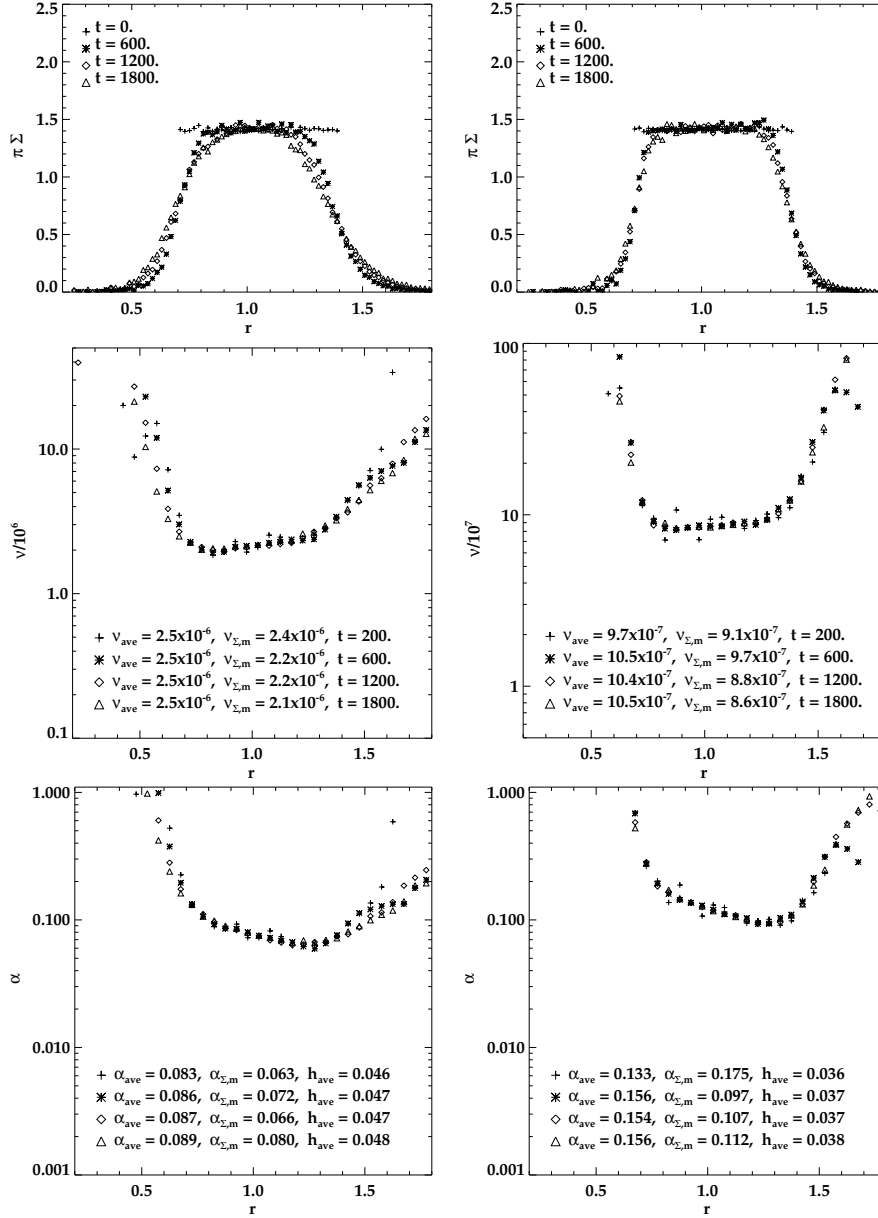


**Figure 4.** Flat-profile discs with constant  $\Sigma_F(x, t = 0)$  (as described in §5.2) and  $N = 5 \times 10^4$ . Left,  $\mu_1 = 60$ ; right,  $\mu_1 = 120$ .

#### 5.4.2 Evaluating the uncorrected artificial viscosity in flows

In switching from  $\Pi'_{ab}$  to  $\Pi_{ab}$  (no Balsara correction), the effective viscosity for  $\alpha_v = 0.8$  is nearly doubled. The clearly linear dependence of  $\alpha_{\Sigma,m}$  and  $\alpha_{ave}$  on  $\alpha_v$  in this case (and with  $\beta_v = 3\alpha_v$ ) is shown for a series of discs in Fig. 6. Best fit lines of the data points are provided as visual guides, with open and skeletal symbols denoting  $\alpha_{ave}$  and  $\alpha_{\Sigma,m}$ , respectively. The dependences on both  $c_s$  and  $h_{ave}$  (which is mainly determined by  $N$ ) remain qualitatively similar to those observed in the Balsara corrected simulations (i.e., increasing either parameter leads to an increase in  $\alpha$ ). In the range of these examples, the ‘empirical’ dependence of the Shakura-Sunyaev  $\alpha$  on SPH and flow parameters can be derived from a fitting procedure similar to that used for Eq. 34 above and given as:

$$\alpha(r) \approx 0.43 \alpha_v \mu(r)^{-1/3} \left[ \frac{h(r)}{2H(r)} \right]^{3/2}. \quad (35)$$

The functional form offers direct insight into the dependences of the effective viscosity on disc parameters, and this relation can be compared with existing approximate, analytic formulae in the literature. Fig. 7 shows a comparison of  $\nu$  derived from Eq. 35 with formulae derived by Murray (1996) and Lodato & Price (2010). Even though the latter two relations were applied for different SPH schemes (as well as containing some dependence on both differing kernels and dimensionality), the figure shows that there are regions of good agreement with the empirical values, namely for small smoothing lengths. (We note that the curves derived in the present study have been restricted to the range of  $h$  values observed in simulations.) However, as  $h$  increases, the differences from the analytic relations increase significantly.

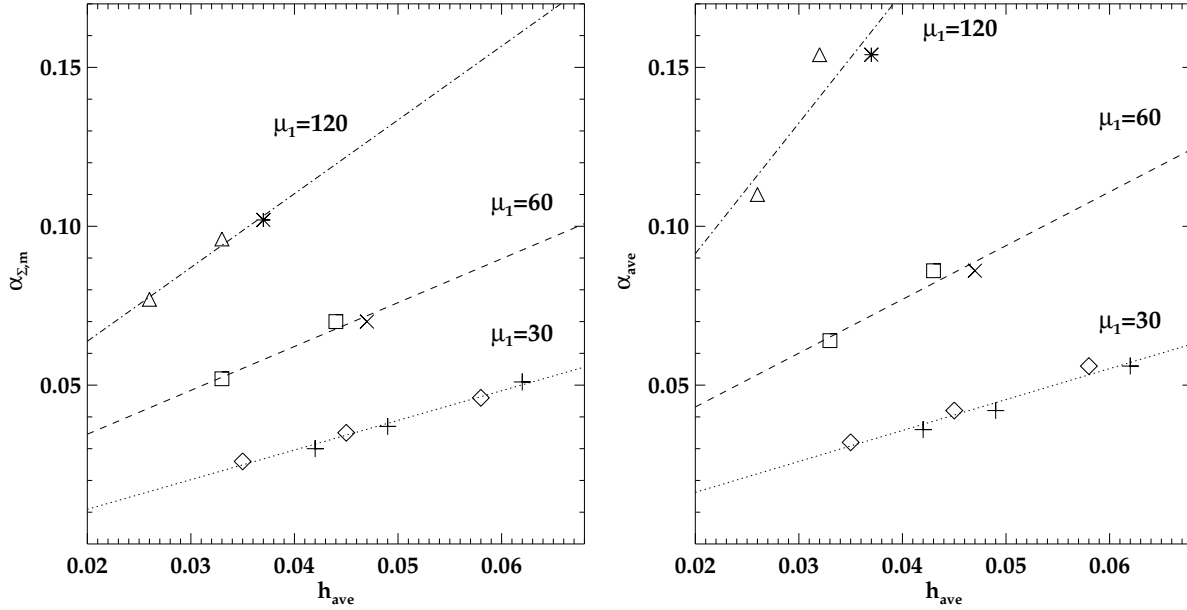


**Figure 5.** Phase space of  $\alpha_{\Sigma,m}$  (left) and  $\alpha_{\text{ave}}$  (right) vs  $h_{\text{ave}}$  from all of the rotating flow simulations in this study using  $\Pi_{ab}^I$  and  $\alpha_v = 0.8$ . Ring and flat-disc simulations ( $\Sigma_R$  and  $\Sigma_F$ ) are represented, respectively, by ‘ $\diamond$ ’ and ‘+’ for  $\mu_1 = 30$ ; by ‘ $\square$ ’ and ‘ $\times$ ’ for  $\mu_1 = 60$ ; and by ‘ $\triangle$ ’ and ‘\*’ for  $\mu_1 = 120$ . The points appear aligned by azimuthal mach number, and best fit lines for  $\mu_1 = 30, 60, 120$  are included as visual guides.

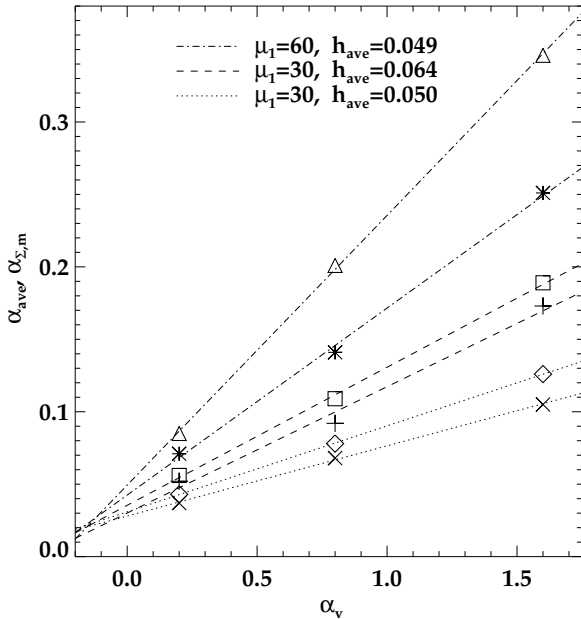


**Figure 6.** Phase space of Shakura-Sunyaev alpha values vs SPH artificial viscosity, using the non-Balsara corrected  $\Pi_{ab}$ . For  $\alpha_v = 0.2, 0.8, 1.6$ ,  $\alpha_{\text{ave}}$  values are respectively shown in open symbols ( $\triangle$ ,  $\square$  and  $\diamond$ ) and  $\alpha_{\Sigma,m}$  values, in skeletal symbols (‘\*’, ‘+’ and ‘ $\times$ ’). The different values of  $\mu_1$  and  $h_{\text{ave}}$  (the latter mainly varying with  $N$ ) are shown on the figure, with best fit lines of the data points as visual guides.

Formulae such as Eq. 35 can be useful in efficiently establishing the setup of a simulation (e.g., choosing the number of particles to produce a required smoothing length, as a sort of resolution requirement). For the non-Balsara flows, extrapolation far beyond the examined parameter space

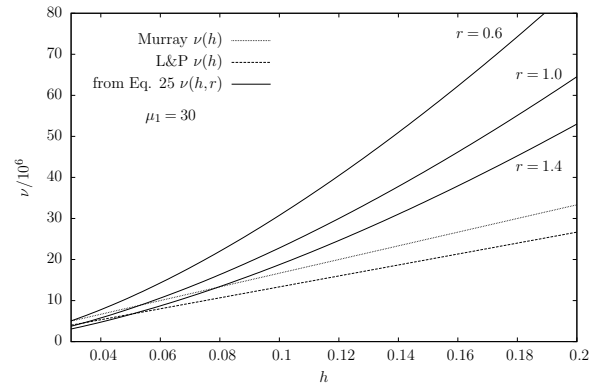


**Figure 7.** A comparison of analytic expressions for the effective disc viscosity,  $\nu$ . Previous analytic expressions from Murray (1996) and from Lodato & Price (2010) are shown with dotted and dashed lines, respectively; solid lines show Eq. 35 for representative radial values. In this ring simulation with  $N = 5 \times 10^4$ , the  $h$  values were mainly between  $3 \times 10^{-2}$  and  $2 \times 10^{-1}$ , hence the displayed interval of the Eq. 35 curves.

with any approximated function is most likely unsuitable. However, a function such as this coming from tests with a fairly wide range of values for the independent quantities may provide an adequate level of accuracy for interpolation.

## 6 SUMMARY AND DISCUSSION

An entropy-based local method has been described to measure the effective kinematic viscosity in the flow due to SPH artificial viscosity, which can be simply related to the Shakura-Sunyaev  $\alpha$  for appropriate thin discs. This approach has several advantages over that of estimating a global  $\nu$  from an isothermal ring-spreading test. First, it

calculates the local viscosity of an annulus from the (viscous) energy or entropy expression, which contains only the term dependent on  $\Pi_{ab}$ , and therefore only viscous effects are measured. This procedure then yields  $\nu$  and  $\alpha$  as functions of radius, so that variations in the effective values across a disc can be determined; global values may be obtained easily via averaging, if desired. In addition, results are generated immediately, without the necessity of finding fits for analytic curves as in ring-spreading, and also thereby eliminating arbitrariness from the estimates. Moreover, the viscosity values are calculated from quantities which are already calculated in the SPH algorithm.

Finally, whereas traditional ring-spreading tests are restricted to use with an isothermal equation of state (or, in practice, even more restricted to cold, 2D systems) because it is only then that one has the analytic solution for comparison, this local method can be used with any equation of state. The effective viscosity may be obtained for rotating flows in general as a function of viscous dissipation, such as from Eq. 26 or 23 (both derived using the very general Eq. 18). The exact form would simply differ from that of Eq. 27, in which a Keplerian profile ( $\Omega = \Omega_K$ ) has been assumed. Further work will also investigate an analogous approach applicable to estimating the effective local shear viscosity for systems in linear motion.

We have compared two existing methods (standard ring-spreading and analytic approximations) with the new, local entropy method in studying the behaviour of the SPH artificial viscosity in rotating flows. In cases where the particular assumptions of the former methods were applicable, average results of all approaches were shown generally to be in fair agreement, with far greater detail coming from the local entropy method. Further examples changing the disc structure and the SPH artificial viscosity values were given. Examples of explicit expressions which approximate the dependence of the numerical  $\alpha$  on various flow and SPH parameters were given for both the Balsara and non-Balsara corrected forms of artificial viscosity. Procedures such as these may provide useful guides when setting up simulations. However, further work must be done to test the generalizability of these specific forms, i.e. Eqs. 34-35, across wider parameter space and to other SPH codes. The means for estimating  $\nu$  and  $\alpha$  in each case, however, applies generally with the local method.

We note that the relations between SPH variables and the effective viscosity in disc flows described here can serve as useful examples of the type of analysis possible with the local entropy measures. The ability for hydrodynamic schemes to represent flows with particular physical viscosity characterizations, such as the widely-used Shakura-Sunyaev discs, may be investigated more directly and in more detail with the local method. Moreover, this analysis may be useful in the further development and evaluation of physically-motivated viscosity terms in SPH, to which existing methods cannot typically be applied. For example, it was shown here that the  $\alpha$  in the case of Balsara corrected artificial viscosity remained finite and linearly dependent on smoothing length. Studies continue to develop schemes for minimizing unwanted effects of artificial viscosity in rotating flows, such as the recent work by Cullen & Dehnen (2010), and we suggest that the simple approach outlined here for measuring the local viscous effects directly would be extremely useful

in quantitatively assessing these developments. (Indeed, we will return to discussion of this in a following paper.)

Finally, several studies have described and investigated numerical implementations of physical viscosity prescriptions derived directly from the analytic Navier-Stokes equations (e.g., Flebbe et al. (1994); Lanzafame, Belvedere & Molteni (2006)), with separate bulk and shear viscosity terms (unlike the standard SPH artificial viscosity, which does not differentiate the two); this is what one must do in order to incorporate real viscosity behaviour into SPH calculations. However, some numerical considerations remain for such physical viscosity prescriptions, in particular regarding spatial derivatives and dependence on particle disorder (see, e.g., Rosswog (2009), as well as Appendix A of the present paper). While one could think of using the SPH artificial viscosity as a model for a real, physical one (see, e.g., the discussion in Sec. 3.2.3. of Lodato & Price (2010)), this provides only a rough approximation, and it is best to think of the present work in terms of establishing acceptable limits for the setup parameters so that the artificial viscosity does not interfere with the effects of the real one.

## 7 ACKNOWLEDGEMENTS

The authors thank Scott Kay, Shazrene Mohamed, Sébastien Peirani, Philipp Podsiadlowski and Stephan Rosswog for useful discussions concerning Gadget-2 and SPH. Many of the computations reported here were performed with the computing cluster at the Centre de Calcul Scientifique at the Université de Sherbrooke, and we thank Lorne Nelson for enabling us to use this. We also gratefully acknowledge support from CompStar, a Research Networking Programme of the European Science Foundation.

## REFERENCES

- Balsara, D. S. 1995, *Journal of Computational Physics*, 121, 357
- Barnes, J., & Hut, P. 1986, *Nature*, 324, 446
- Bate, M. R., & Burkert, A. 1997, *MNRAS*, 288, 1060
- Boss, A. P., & Bodenheimer, P. 1979, *ApJ*, 234, 289
- Cha, S.-H., & Whitworth, A. P. 2003, *MNRAS*, 340, 73
- Cullen, L., & Dehnen, W. 2010, *MNRAS*, 408, 669
- Flebbe, O., Muenzel, S., Herold, H., Riffert, H., & Ruder, H. 1994, *ApJ*, 431, 754
- Frank, J., King, A., & Raine, D. J. 2002, *Accretion Power in Astrophysics*. Cambridge, UK: Cambridge University Press, 2002.
- Gingold, R. A., & Monaghan, J. J. 1977, *MNRAS*, 181, 375
- Herant, M. 1994, *Memorie della Società Astronomia Italiana*, 65, 1013
- Imaeda, Y., & Inutsuka, S.-i. 2002, *ApJ*, 569, 501
- Inutsuka, S.-I. 2002, *Journal of Computational Physics*, 179, 238
- Landau, L. D., & Lifshitz, E. M. 1959, *Course of theoretical physics*, Oxford: Pergamon Press, 1959
- Lanzafame, G., Belvedere, G., & Molteni, D. 2006, *A&A*, 453, 1027
- Lodato, G., & Price, D. J. 2010, *MNRAS*, 405, 1212

- Lucy, L. B. 1977, *AJ*, 82, 1013
- Lüst, R. 1952, *Zeitschrift Naturforschung Teil A*, 7, 87
- Lynden-Bell, D., & Pringle, J. E. 1974, *MNRAS*, 168, 603
- Monaghan, J. J. 1997, *Journal of Computational Physics*, 136, 298
- Monaghan, J. J. 2005, *Reports of Progress in Physics*, 68, 1703
- Monaghan, J. J. 2006, *MNRAS*, 365, 199
- Murphy, J. W., & Burrows, A. 2008, *ApJS*, 179, 209
- Murray, J. R. 1996, *MNRAS*, 279, 402
- Navarro, J. F., & White, S. D. M. 1993, *MNRAS*, 265, 271
- Price, D. J. 2010, arXiv:1012.1885
- Pringle, J. E. 1981, *Annual Review of Astronomy and Astrophysics*, 19, 137
- Rosswog, S., Speith, R., & Wynn, G. A. 2004, *MNRAS*, 351, 1121
- Rosswog, S. 2009, *New Astronomy Reviews*, 53, 78
- Shakura, N. I., & Sunyaev, R. A. 1973, *A&A*, 24, 337
- Speith, R., & Riffert, H. 1999, *Journal of Computational and Applied Mathematics*, 109, 231
- Speith, R., & Kley, W. 2003, *A&A*, 399, 395
- Springel, V., & Hernquist, L. 2002, *MNRAS*, 333, 649
- Springel, V. 2005, *MNRAS*, 364, 1105
- Steinmetz, M. 1996, *MNRAS*, 278, 1005
- Szuskiewicz, E., & Miller, J. C. 1997, *MNRAS*, 287, 165
- Tassoul, J.-L. 1978, *Princeton Series in Astrophysics*, Princeton: University Press, 1978,
- Taylor, P. A., Miller, J. C., & Podsiadlowski, P. 2011, *MNRAS*, 410, 2385
- Toomre, A. 1964, *ApJ*, 139, 1217
- Truelove, J. K., Klein, R. I., McKee, C. F., Holliman, J. H., II, Howell, L. H., Greenough, J. A., & Woods, D. T. 1998, *ApJ*, 495, 821

## APPENDIX A: INITIAL PARTICLE DISTRIBUTION

As any SPH simulation evolves, the particles asymptotically tend toward an equilibrium of mutual separation distances (i.e., no artificial clumps or voids) within the local profile (Monaghan 2006). The presence of either lattice-regularity or purely random (over)density fluctuations in the initial conditions impedes this process, resulting instead in purely numerical features, the effects of which may continue to propagate in the simulated flows, e.g., Imaeda & Inutsuka (2002); Monaghan (2006). For example, locating SPH particles at regular gridpoints often leads to spurious spiral modes in rotating systems (though ‘real’ spirals may form due to susceptibility conditions in certain cases, such as those given by Toomre (1964); Speith & Kley (2003)). In particle setup methods using random placements of equal-mass particles, some of these numerical side effects are limited, but fluctuations may still occur in the flow which are of an entirely artificial nature, particularly due to localised overdensities; typical solutions of these difficulties have been to enforce a minimum initial separation between randomly placed particles (a computationally expensive,  $N^2$  procedure which is not guaranteed to remove all fluctuations), as well as spending time at the beginning of a simulation to evolve the system in the presence of strong damping, while maintaining the desired profiles of density, velocity, energy, etc.

(Rosswog, Speith & Wynn 2004; Monaghan 2006; Rosswog 2009).

In this work, we have utilised a new method to create equal-mass particle distributions which are both smooth and random (SAR) from the start of a simulation, i.e., limiting numerical fluctuations due to initial placement. The SAR method produces such conditions at  $t = 0$ , without the need for special runtime considerations (such as damping, etc.) during the simulation. There is very little fixed cost in creating such a distribution, and neither damping nor further non-hydrodynamic numerics are introduced into the model. The SAR method for setting up initial conditions is valid for any number of dimensions and does not assume any particular symmetries.

### A1 SAR process steps

To make SAR initial conditions for a simulation, an intermediate distribution of point particles is first created, called a ‘glass’. The glass is defined by the property that its constituent particles are equidistant from their nearest neighbours but without regular structure (such as in a crystal). For practical considerations of generating a glass, it is computationally efficient to first make a single, small glass distribution and then to tile copies with periodic boundaries appropriately matched to preserve interparticle spacing.

The general process of creating an SAR particle distribution may be divided into the following steps:

- (i) seed a mini-glass distribution: place a small number,  $N_g$ , of point particles randomly in a cube of normalised edge length,  $L_g = 1$ , with periodic boundaries
- (ii) create the mini-glass: evolve the particles with mutually repulsive (here, inverse-square) forces, asymptotically approaching a constant density of equidistant particles (particle velocity is zeroed after each timestep to limit ‘over-shooting’ equilibrium)
- (iii) create full glass: tile copies of the mini-glass cubes (into any given size/shape), with the periodic boundaries of tiles matched to preserve particle spacing
- (iv) fill simulation model: select a small volume of the glass (including particles) and map it into the model, adjusting the element volume (and relative particle locations therein) to the local density of the profile by compressing or stretching it
- (v) repeat the previous step, smoothly mapping neighbouring volumes from the glass to neighbouring volumes in the model profile, maintaining an absence of spurious particle number density fluctuations.

Using small volumes, such a process preserves the relative spacing of all points while creating an appropriate density profile.

### A2 Testing the SAR distributions

Here, we first tested a SAR distribution model using a standard SPH test of particle resolution and convergence: the collapse of a self-gravitating, isothermal sphere initially in solid body rotation and with a non-axisymmetric ( $m = 2$ ) density perturbation. The system fragments, and this has been well-examined using both Lagrangian

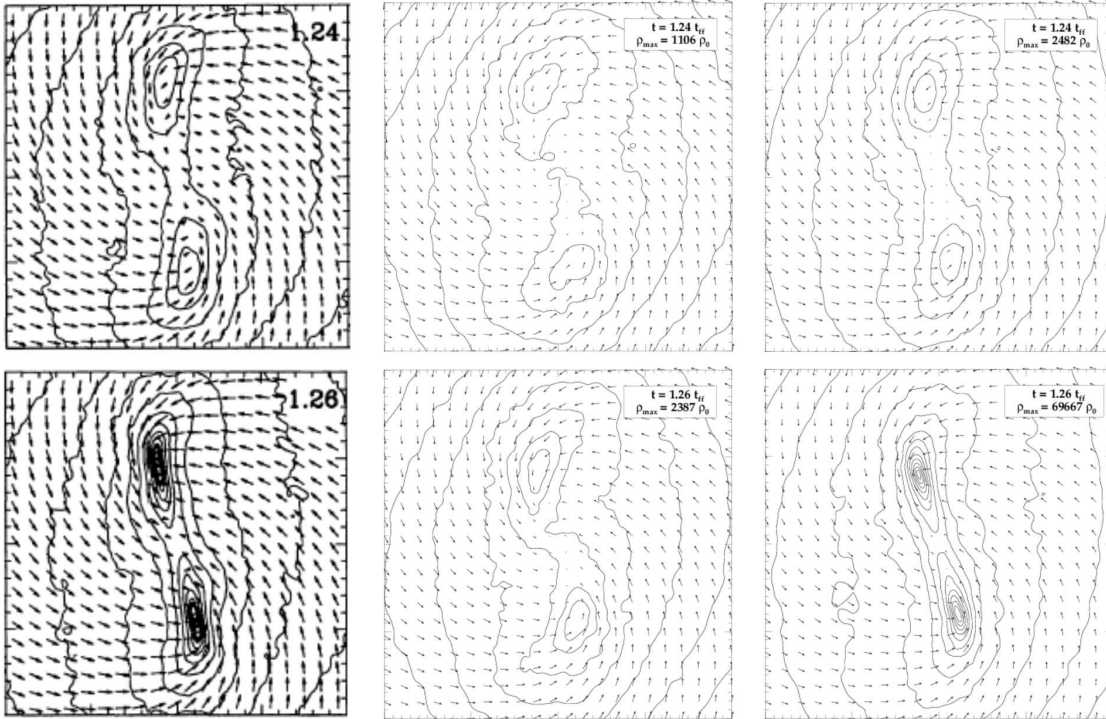


**Figure A1.** Isothermal sphere test (equatorial) density contours with four density contours are drawn per decade. Col. 1: ‘solution’ from Fig. 4 of Bate & Burkert (1997), for which  $N = 8 \times 10^4$ ; peak densities at  $t = 1.24$  and  $1.26$  are  $\rho_{\max}/\rho_0 \approx 2,400$  and  $78,500$ , respectively. Cols. 2 and 3: NEM and SAR distribution simulations, respectively; in both,  $N = 6.7 \times 10^4$ . SAR results show much greater agreement with the first column ‘solution’, both qualitatively and quantitatively.

and various Eulerian grid codes (Boss & Bodenheimer 1979; Bate & Burkert 1997; Truelove et al. 1998). SAR models were tested with total particle number  $N = 3.4 \times 10^4$ ,  $6.7 \times 10^4$  and  $2 \times 10^5$ , and results were compared with lattice-like, nonequal mass (NEM) placements using a standard configuration (e.g. Springel (2005)) at similar resolutions. Results of both simulations were also compared with convergent ‘solution’ results of Bate & Burkert (1997).

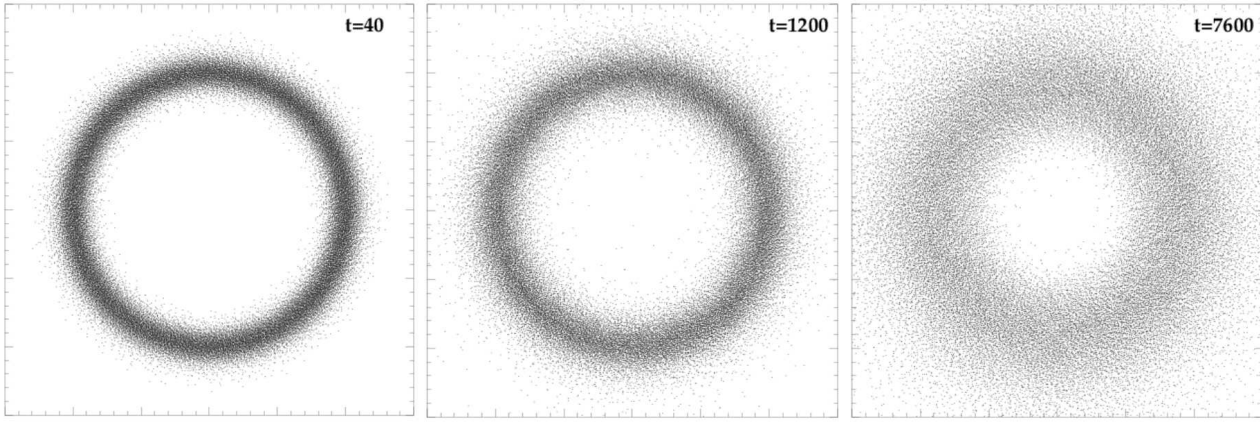
Briefly, the initial conditions of the test are: at  $t = 0$ , we start with an isothermal ( $P = c_s^2 \rho$ ) sphere having uniform sound speed,  $c_s = 1.66 \times 10^4$  cm s $^{-1}$ ; radius,  $R_S = 5 \times 10^{16}$  cm; mass,  $M = 1M_\odot$ ; and solid body angular velocity,  $\omega = 7.2 \times 10^{-13}$  rad s $^{-1}$ . The density distribution has an  $m = 2$  perturbation over the azimuthal angle given by  $\rho(\phi) = \rho_0[1 + 0.1 \cos(2\phi)]$ , where  $\rho_0 = 3.82 \times 10^{-18}$  g cm $^{-3}$ . All quantities in this section are scaled by the following characteristic quantities: the initial value of the outer radius,  $R_S$ ; the free-fall time,  $t_{\text{ff}} = (3\pi/32G\rho_0)^{1/2}$ ; and the mass,  $M_\odot$ .

Fig. A1 shows plots of density in the equatorial plane of the SAR and NEM distributions with  $N = 6.7 \times 10^4$  particles, as well as the convergent ‘solution’ (top), at  $t = 1.24$  and  $1.26$ . Quantitatively, the peak density of the SAR simulation was much closer to the expected value than that of the NEM case (and at fairly low resolution). This remained true for all  $N$  values investigated, and furthermore, the SAR contours were significantly smoother and more ‘fluidlike’ with fewer numerical fluctuations. The simulation results using SAR conditions converged much more quickly to the expected results as resolution was increased, an important property for creating efficient simulations.

As an additional example of SAR results, Fig. A2 shows images of particle locations for an evolving SAR ring simulation (the same system as in the left panel of Fig. 3), projected onto the equatorial plane. Over time, the particle distribution within system retains its good qualitative properties of smoothness and randomness. Note the absence of any temporary artificial spirals, clumps or sub-structures, such as often appear in SPH simulations, even at very early times. Both the efficiency of modelling and the relative ease of formulation (the computation requires only a few simple loops through  $N$  particles), in addition to a reduction of numerical artefacts, make the SAR initial conditions very beneficial for use in SPH simulations.

Importantly, the SAR particle method is effective because the quasi-continuous mapping retains the relative spacing between particles from the initial glass<sup>2</sup>. The new density profile is obtained smoothly and accurately, without the presence of fluctuations or numerical artefacts. How smoothly a density profile is reproduced is principally determined by the size of the incremental volume element. The SAR method does result in a small amount of localised asymmetry in the particle distribution, as volume elements are not generally scaled uniformly in all directions, but for

<sup>2</sup> A version of particle setup obtained by warping a constant density profile (Herant 1994) has been pointed out by a referee. Although the mapping feature therein is ostensibly similar to what is described here, that method was limited for use with a certain subset of spherically symmetric profiles and was made from uniformly placed (not SAR) particles.



**Figure A2.** A sequence of positions of SPH particles, projected onto the equatorial plane, for the  $\mu_1 = 60$ ,  $N = 5 \times 10^4$  model shown in the left column of Fig. 3. Note the early and continued absence of clumps, voids and temporary spiral.

small elements this did not appear to produce spurious artefacts during simulations. Improvements to the method are currently being considered.